The Structure and Energetics of Midlatitude Disturbances Accompanying Cold-Air Outbreaks over East Asia

NGAR-CHEUNG LAU

Geophysical Fluid Dynamics Program, Princeton University, Princeton, NJ 08540

KA-MING LAU

Goddard Laboratory for Atmospheric Sciences, NASA/Goddard Space Flight Center, Greenbelt, MD 20771

(Manuscript received 27 October 1983, in final form 12 March 1984)

ABSTRACT

The onset dates for 11 individual cold-air outbreaks over the East Asian seaboard during the Winter Monsoon Experiment (1 December 1978–28 February 1979) are used for constructing composite synoptic charts. The three-dimensional structure and energetics of disturbances with time scales shorter than ~ 5 days are distinguished from the corresponding properties of more slowly varying fluctuations by using time-filtering techniques.

It is seen that the high-frequency disturbances accompanying the cold surges experience systematic structural changes as they migrate along a well-defined storm track from East Asia to the Gulf of Alaska. The typical life cycle of such extratropical storms is characterized by a baroclinic growth phase coinciding with the polar outbreaks, and a decay phase in which barotropic processes play an active role. The propagation of low-frequency fluctuations is oriented toward lower latitudes, with new vorticity centers developing downstream and equatorward of the primary disturbances associated with the outbreaks. The shapes of the disturbances appearing in the composite charts indicate that a strong degree of anisotropy exists in both the high-frequency and low-frequency disturbances. The fluctuations with short time scales are elongated in the meridional direction, whereas those with long time scales are elongated in the zonal direction.

The findings of this composite study are seen to be consistent with circulation statistics derived from continuous climatological records. The behavior of the fluctuations with short and long time scales is also reminiscent of the characteristics of baroclinically unstable waves and Rossby-wave trains, respectively, appearing in model experiments.

1. Introduction

Among the most striking synoptic phenomena of the wintertime circulation over the East Asian seaboard are the incursions of cold air masses from the continental interior. These cold-air outbreaks are mostly characterized by an abrupt drop in the surface temperature and a marked intensification of the prevalent low-level flow associated with the East Asian winter monsoon. The severe weather accompanying the intense cold surges often brings about major disruptions of agricultural and economic activities in the affected regions. The abruptness of the onset of such outbreaks and the considerable economic costs involved have spurred the need for accurate forecasts of the incidence of cold surges in this region. It was in recognition of this need that the winter phase of the Monsoon Experiment (MONEX) in 1978–79 included among its principal objectives a comprehensive understanding of the nature of these cold surges. A survey of our current knowledge of various phenomena associated with the East Asian monsoon was recently made by Lau and Li (1984), who also highlighted the important contributions to this problem made by the meteorological communities in China, Japan and other countries in that region.

The case study by Chang *et al.* (1979) has provided observational evidence on the extensive air–sea interaction and organized convective activity which occcur over the near-equatorial South China Sea following northeasterly cold surges over that region. Subsequent studies by Chang and Lau (1980, 1982) demonstrated that the active surge periods are accompanied by a strengthening of the local, thermally direct meridional circulation over East Asia, and by noticeable fluctuations in the intensity of Walker-type circulations in the near-equatorial zonal plane. More recently, Lau *et al.* (1983) further showed that downstream development associated with the cold surges often leads to enhancement of near-equatorial convection over the central Pacific. Observational studies by other investigators indicate that, in addition to being closely related to atmospheric conditions in the tropics and subtropics, the outbreak episodes are preceded as well as followed by significant circulation features in middle and higher latitudes. Joung and Hitchman (1982) have noted the

presence of organized wave trains over the extratropical North Atlantic as much as 6–7 days prior to the occurrence of intense polar outbreaks over Korea. Successive downstream development of these disturbances is clearly evident along a well-defined track extending eastward all the way from the east coast of the United States to the central Pacific.

The observational studies cited above suggest that not only do these outbreak episodes affect the local weather in a significant way, but also they are associated with changes in the planetary-scale circulation. The cold surge phenomenon is hence seen to be just one regional manifestation of an extended family of atmospheric processes with far-reaching effects.

One of the most recognizable synoptic features related to the outbreaks is the pronounced enhancement of baroclinicity over the East Asian seaboard. This phenomenon is largely brought about by the penetration of polar continental air masses toward a much warmer maritime environment. Such local strengthening of the thermal contrast is in turn accompanied by acceleration of the semipermanent East Asian jet stream. Observational studies by Blackmon *et al.* (1977), Lau (1979) and others have demonstrated that active transient disturbances tend to develop downstream of the climatological jet over East Asia. These findings suggest that the intensification of this jet stream during the cold surges is likely to be followed by pronounced wave activity over the western and central Pacific. Hence the times and locations of cold-air outbreaks over East Asia should provide a convenient frame of reference for composite studies of the characteristic structure and development of the wave disturbances prevalent in that region.

This work is aimed at delineating the evolution of extratropical transient waves as they propagate eastward from the Eurasian land mass toward the Pacific during selected cold surge events in the winter MONEX period. An approach basically similar to that of Joung and Hitchman (1982) is adopted here. However, the efforts of the present study are mostly concentrated on documenting the three-dimensional structure and energetics of the transient waves at various stages of their development, and on distinguishing the behavior of disturbances with different time scales. The insights to be gained from this case study should aid the interpretation of results presented by Blackmon *et al.* (1977, 1984a,b), who investigated similar phenomena by applying statistical techniques to continuous climatological records. The empirical findings reported here are probably also of interest to current modeling and theoretical studies on the temporal evolution of various types of wave motion in middle latitudes.

The outstanding cold surge episodes during the winter MONEX period are identified in Section 2, which also contains a brief description of the data set and analysis procedures used in this study. The salient synoptic features related to the cold surge events are described in Section 3 using composite streamline charts. The structure of rapidly varying disturbances accompanying the cold surges, and the associated energetics, are examined in Section 4. The material in Section 5 is devoted to the behavior of those fluctuations with relatively longer time scales. The findings of this study are summarized and discussed in Section 6.

2. Data sets and analysis procedures

a. Data sets

The observational data base for this study consists of twice-daily global analyses of geopotential height, wind and temperature at ten standard pressure levels from 1000 to 100 mb during winter MONEX (1 December 1978–28 February 1979). These analyses were produced by the National Meteorological Center on an operational basis, and are also designated as FGGE Level III-A data. The horizontal resolution of the data grids is 2.5° in both the zonal and meridional directions. The daily station records described in Section 2c were made available to us through the kind arrangements of Mr. Zou Jingmeng, Administrator of the State Meteorological Administration, Peoples' Republic of China.

b. Time filters

A nine-point Gaussian-type low-pass filter has been designed to differentiate synoptic phenomena occurring on time scales less than ~ 5 days from the much more slowly varying fluctuations. For observations x_0 taken at 12-hour intervals, the low-pass filtered value x_l and the high-pass filtered value x_h at time t_i are given by

$$x_l(t_i) = a_0 x_0(t_i) + \sum_{p=1}^{4} a_p[x_0(t_{i+p}) + x_0(t_{i-p})],$$

$$x_h(t_i) = x_0(t_i) - x_l(t_i).$$

Values of the weights a_p are given in Table 1, and the frequency response of the above operations is presented in Fig. 1. The filtering weights used here are essentially proportional to the ordinates of the normal probability curve for a standard deviation of 1 day [see Holloway, 1958, Eq. (5.10)].

c. Identification of the cold surge episodes during winter MONEX

As mentioned in the Introduction, cold surges over the East Asian seaboard are mostly identified by noting changes of the following indicators within a 24- to 48-

TABLE 1. Values of the weights a_p used for constructing the low-pass and high-pass filters in this study.

a_0	0.2041636
a_1	0.1801738
a_2	0.1238316
a_3	0.0662822
a_4	0.0276306

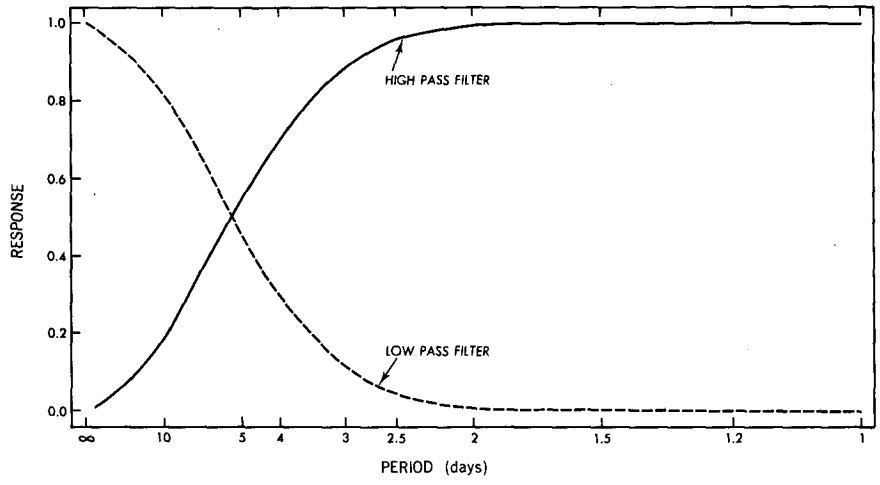

FIG. 1. Frequency responses of the high-pass filter (solid curve) and low-pass filter (dashed curve) used in this study.

hour period: a drop in the surface temperature of 5°C or more, an increase of at least 5 mb in the surface pressure gradient between the coast and central China, and a prevalent northerly surface flow with speeds exceeding 5 m s^{-1}. An analogous set of criteria have been used in the winter MONEX field phase report (GARP, 1980) for defining cold surges over the South China Sea. Figure 2 shows the variation within the period from 1 December 1978 to 28 February 1979 of the daily mean surface temperature at the coastal stations Canton (Guangzhou; 23°N, 113°E), Foochow (Fuzhou; 26°N, 119°E) and Shanghai (31°N, 121°E), as well as the differences between the daily mean surface pressure at the inland station Wuhan (30°N, 114°E) and at the coastal stations. Those dates when the local surface wind has a northerly component and the wind speed exceeds 5 m s^{-1} are indicated in the top three panels by heavy dots. Some lagged cross-correlations between the time series in Fig. 2 are presented in Table 2. It is seen that the temperature variations at Shanghai tend to lead by about 1 day the corresponding changes at coastal stations located farther south, thus indicating a general tendency for the influence of cold surges to spread equatorward. The results shown in Fig. 2 and Table 2 also suggest that a sharp rise in the pressure differential between Wuhan and the coast tends to occur about 1 day prior to the temperature surge at the coast. By applying the criteria outlined earlier in this paragraph, as well as by inspection of both Fig. 2 and the sequence of daily synoptic charts for the periods of interest, it is possible to identify 11 cold surge episodes. In this study, the specific reference date and time for each event is taken to be the instant when the cold-air outbreak over the East Asian seaboard reached its maximum spatial extent. These key dates, which are listed in Table 3 and depicted in Fig. 2 by shaded stripes, provide the basis for constructing the composite charts to be shown in later sections. It is evident from the station data in Fig. 2 that, in each of the 11 cases chosen here, nearly all indicators at all stations satisfy the selection criteria for cold surges mentioned above. However, most of the surges during winter MONEX are of moderate strength, and only a few of the events in this period are as severe as those examined by Joung and Hitchman (1982). The key dates for the present study are similar to those used by Lau *et al.* (1983). The minor discrepancies between the two sets of key dates arise from the different definitions used.

d. Construction of composite charts

The key date and time for each surge event listed in Table 3 is labeled as "Day 0". The dates and times for the 6-day period centered on each key date are categorized as "Day −3", "Day −2.5", . . . , "Day −0.5", "Day 0", "Day +0.5", . . . , "Day +2.5" and "Day +3". Here the minus (plus) sign indicates times preceeding (following) the key date. Hence there are 13 such time categories for twice-daily observations. Composite charts are constructed by averaging over the 11 cases the filtered or unfiltered data for the same time category. Since some of the key dates are separated from each other by rather short time intervals, some overlapping of their respective 6-day composite periods is inevitable. The resulting ambiguities are partially removed by rejecting all data beyond the time category which falls within 1 day of the previous or the next key date.

3. General synoptic description

Figure 3 shows composite streamline/isotach charts for (a) Day −1.5, (b) Day 0 and (c) Day +1.5. These charts were constructed using unfiltered wind data at 500 mb. Prior to the cold surges (Fig. 3a), a straight zonal flow prevails over the East China Sea and the western Pacific. The circulation upstream from the Asian coast on Day −1.5 is marked by the presence

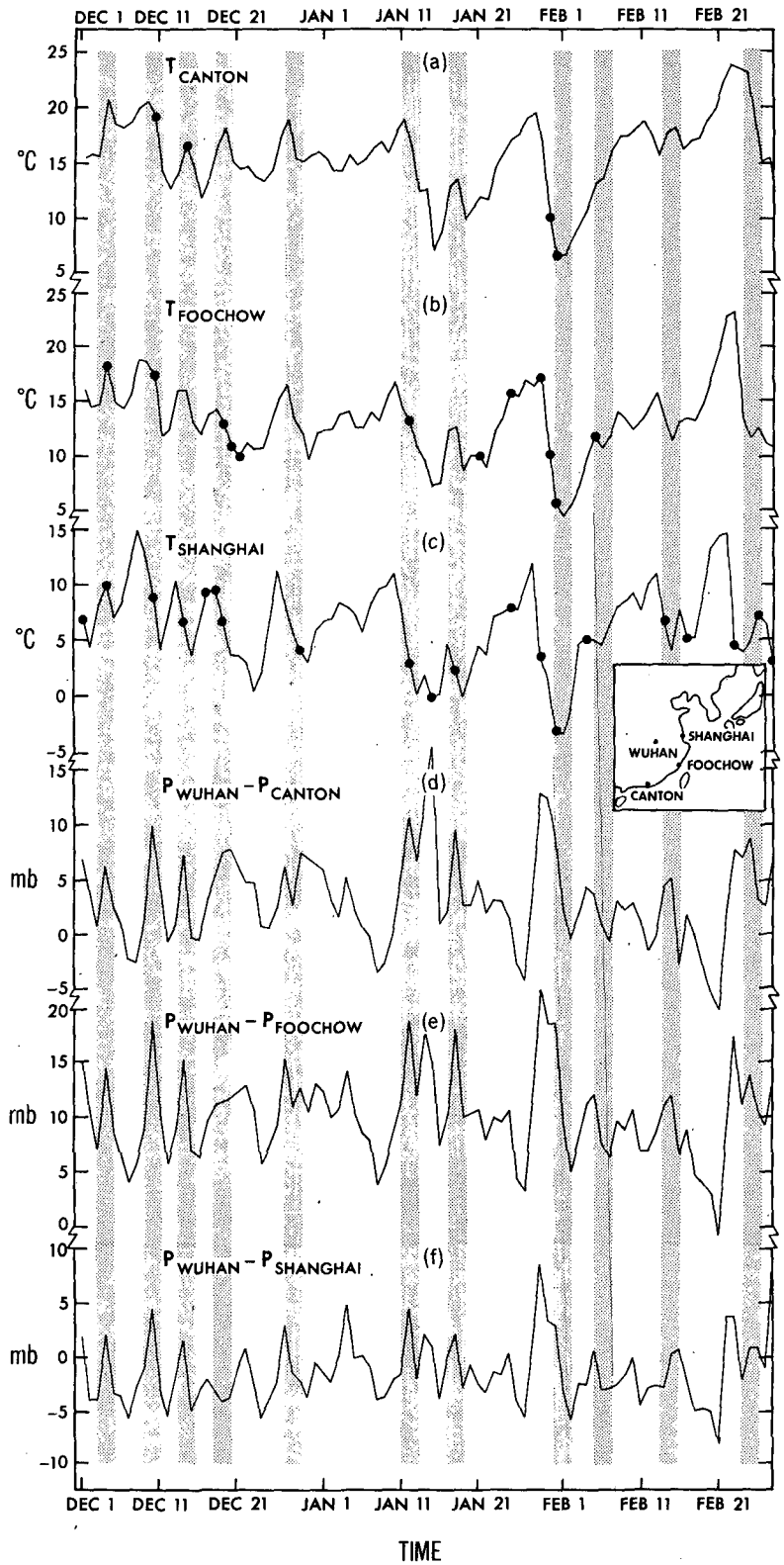

FIG. 2. Time series of daily averaged surface temperature for the 1978–79 winter at (a) Canton, (b) Foochow and (c) Shanghai, and of differences in daily averaged surface pressure between Wuhan and (d) Canton, (e) Foochow and (f) Shanghai. The heavy dots in panels (a), (b) and (c) indicate all days within the 1978–79 winter when the local surface flow has a northerly component and the wind speed exceeds 5 m s^{-1}. The shaded stripes indicate the cold surge episodes used for constructing composite charts. The locations of the stations are indicated in the inset map.

TABLE 2. Values of selected temporal correlation coefficients between the daily mean surface temperatures at Canton (T_C), Foochow (T_F) and Shanghai (T_S), as well as differences between the daily mean surface pressure at Wuhan and the corresponding value at Canton ($P_W - P_C$), Foochow ($P_W - P_F$) and Shanghai ($P_W - P_S$), for the 1978–79 winter. The number in parentheses to the right of each correlation coefficient indicates the time lag used in computing that particular statistic: +1 (−1) indicates that the time series for the meteorological variable given at the top of the column leads (lags) the time series for the variable given at the head of the row by 1 day; 0 indicates zero lag.

	T_F	T_S	$P_W - P_C$	$P_W - P_F$	$P_W - P_S$
T_C	0.76 (+1) 0.85 (0) 0.69 (−1)	0.79 (+1) 0.72 (0) 0.47 (−1)	−0.54 (+1) −0.20 (0) 0.01 (−1)		
T_F		0.85 (+1) 0.80 (0) 0.45 (−1)		−0.58 (+1) −0.07 (0) 0.12 (−1)	
T_S					−0.58 (+1) −0.12 (0) 0.17 (−1)
$P_W - P_C$				0.92 (0)	0.67 (0)
$P_W - P_F$					0.85 (0)

of a prominent pressure ridge centered at about 90°E (labeled A in Fig. 3a), and a weak trough to the east. The ridge A is clearly discernible northeast of the Caspian Sea on Day −3 (not shown), and undergoes considerable amplification as it progresses steadily eastward from Day −3 to Day −1. On Day 0 (Fig. 3b), the trough located east of A deepens rapidly as it passes over the East Asian seaboard. This rather sudden development is accompanied by noticeable wind accelerations south and east of the intensifying trough (labeled B in Figs. 3b and c). During the next 36 hours this trough migrates steadily toward the western Pacific. On Day +1.5 (Fig. 3c), the trough axis has developed a southeast–northwest tilt north of the jet stream, and a southwest–northeast tilt farther south. Another notable feature in Fig. 3c is the deep pressure trough C centered at the Date Line over the subtropical Pacific. The development of this midocean trough starts on Day +1, and it remains quasi-stationary through Day +2.5.

TABLE 3. Dates and times for the onset of cold surges over East Asia during the 1978–79 winter.

Date	Time (GMT)
4 December 1978	1200
10 December 1978	1200
14 December 1978	0000
19 December 1978	0000
28 December 1978	0000
12 January 1979	1200
18 January 1979	1200
1 February 1979	0000
6 February 1979	0000
15 February 1979	0000
25 February 1979	1200

The surface circulation on Day 0 is portrayed in Fig. 4 by a composite streamline/isotach chart, which is constructed using unfiltered data at 1000 mb. The cold surges over East Asia are seen to be typically accompanied by the appearance of an intense cyclone–anticyclone pair over that region. Examination of the sequence of surface maps for individual outbreaks typically indicates the passage of a well-defined cold front across the Southeast Asian seaboard during the period from Day −1 to Day 0. The genesis of a high pressure center over the Chinese mainland (H in Fig. 4) and a low pressure center over Japan (L) occur almost spontaneously during the same period. On Day 0, northerly surface winds prevail over the entire eastern seaboard, with maximum speeds approaching 15 m s^{-1} over the East China Sea. The cyclone center over Japan advances steadily northeastward and may be traced all the way to the Bering Sea during the next 72 hours. The well-defined track followed by this composite cyclone is depicted in Fig. 4 by the dashed arrow.

4. Evolution of fluctuations with short time scales

a. Three-dimensional structure

The typical horizontal structure of rapidly varying disturbances at different stages of the cold-air outbreaks is illustrated by the composite charts of high-pass filtered (see Section 2b) 500 mb height data on Days −1, 0, +1, +2 and +3, shown in Fig. 5. The geopotential height fluctuations shown here (and in Figs. 7, 8a and b, 12 and 13a) are weighted by the factor sin 45°/sinϕ, where ϕ is latitude, so that these patterns may be interpreted as depicting the geostrophic streamfunction. In order to track the movement of individual ridges and troughs during different composite times, the labels R_1, R_2 (for ridges) and T_1, T_2

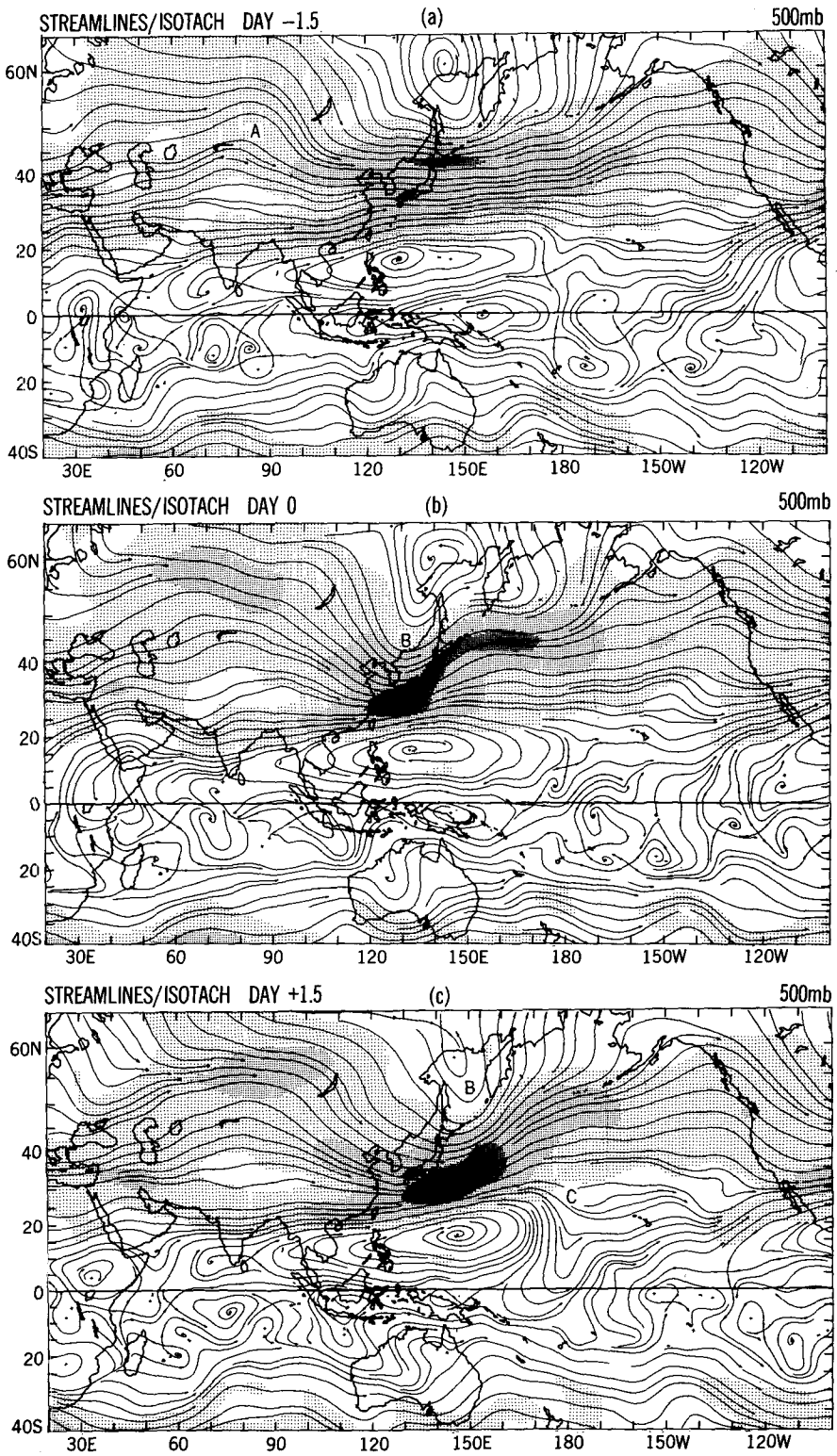

FIG. 3. Composite streamline charts at 500 mb on (a) Day −1.5, (b) Day 0 and (c) Day +1.5. The local wind speeds are depicted by various degrees of shading: 0–10 m s^{-1} (no shading), 10–20 m s^{-1} (light shading), 20–30 m s^{-1} (medium shading) and >30 m s^{-1} (dark shading). The labels A, B and C identify synoptic features discussed in the text.

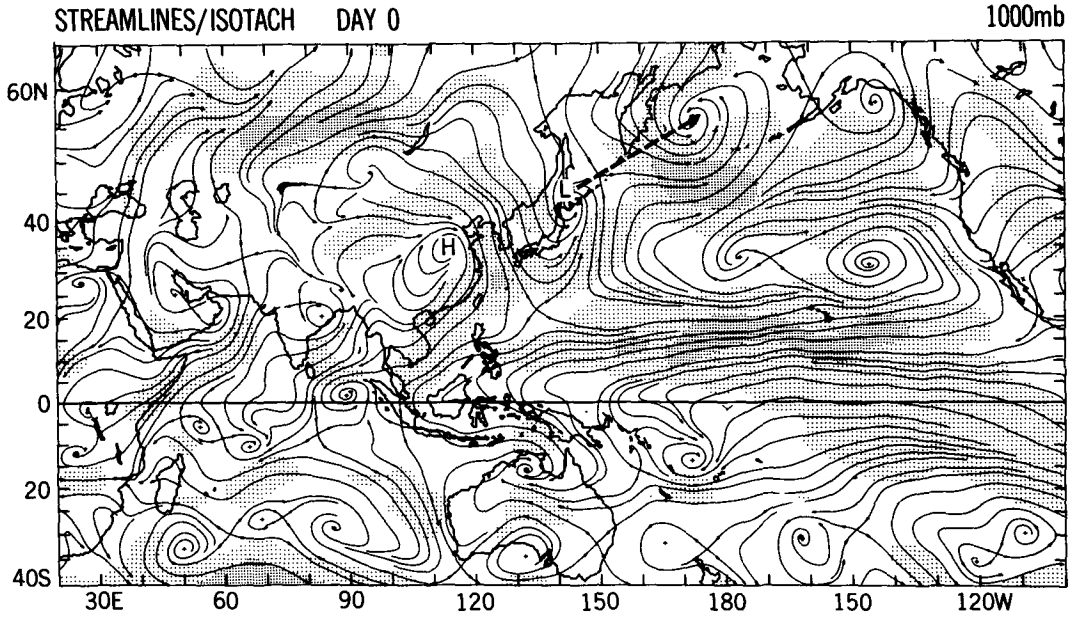

FIG. 4. Composite streamline charts at 1000 mb on Day 0. The local wind speeds are depicted by various degrees of shading: 0–5 m s^{-1} (no shading), 5–10 m s^{-1} (light shading) and 10–15 m s^{-1} (medium shading). Letters L and H identify the cyclone–anticyclone pair associated with the cold surges. The composite track of the low pressure center during the following 72 hours is depicted by the dashed arrow.

(for troughs) are assigned to local maxima and minima, respectively, in Fig. 5. It is seen from Fig. 5 that these features exhibit a strong temporal continuity. The distribution on Day −1 (Fig. 5a) is rather representative of the synoptic pattern during Day −3 through Day −1. Prior to the outbreaks, the most active high-pass fluctuations are located over the northern portion of the Eurasian land mass and Japan, with comparatively weak amplitudes. As these disturbances migrate southeastward and approach the eastern seaboard, their axes tend to acquire a characteristic southwest–northeast tilt, as is evident from the shape of the ridge R_1 in Fig. 5a, and the composite streamlines in Fig. 3a. On Day 0 (Fig. 5b), the train of waves becomes much more organized. The circulation over the eastern edge of the continent is dominated by a pronounced trough T_1. During the subsequent days, the group of disturbances move primarily northeastward in the direction of the Aleutian Islands. Considerable amplification of the individual troughs and ridges also takes place between Day −1 and Day +1. The horizontal structure of the mature disturbances over the North Pacific on Days +1 and +2 (Figs. 5c and d) is characterized by a pronounced southwest–northeast tilt of the trough and ridge axes south of ~45°N, and a southeast–northwest tilt farther north. These high-pass perturbations have typical zonal wavelengths of 4000–5000 km, and are distinctly elongated in the meridional direction. The characteristic shape of the synoptic scale waves over the oceanic storm tracks, as revealed by the composite charts displayed here, is in good agreement with the findings of Blackmon *et al.* (1984a,b) who used cross-correlation techniques, and of Hoskins *et al.* (1983) who used anisotropy measures. The characteristic horizontal tilts of the composite waves are consistent with the prevalence of poleward transport of westerly momentum by synoptic scale transient eddies south of the storm tracks, and equatorward transport farther north, as is evident in the climatological circulation statistics presented by Blackmon *et al.* (1977, Fig. 7b). The observed structure of the mature disturbances is also qualitatively similar to that of the principal modes of instability for a three-dimensional flow typical of the Northern Hemisphere winter, as presented by the numerical study of Frederiksen (1983, Fig. 9). By Day +3 (Fig. 5e), the composite disturbances are considerably weakened as they traverse the North Pacific, and they become much less organized compared with the developing stage. With the possible exception of the brief appearance of a subtropical feature centered at 22°N, 175°W on Day +2 (Fig. 5d), the activity of the high frequency waves is mostly confined to the region poleward of 30°N.

The track of the individual maxima and minima described in Fig. 5 is constructed by connecting the positions of R_1, R_2, T_1 and T_2 at different composite times, and is represented by the bold line in Fig. 6. This track is hereafter referred to as the "storm track". Superimposed on the same figure is the distribution of 500 mb height averaged over the period from Day −3 to Day +3 for all 11 cases. This pattern may be viewed as the large scale, quasi-stationary flow field in which the high-pass fluctuations are embedded. The close alignment of the storm track with the orientation

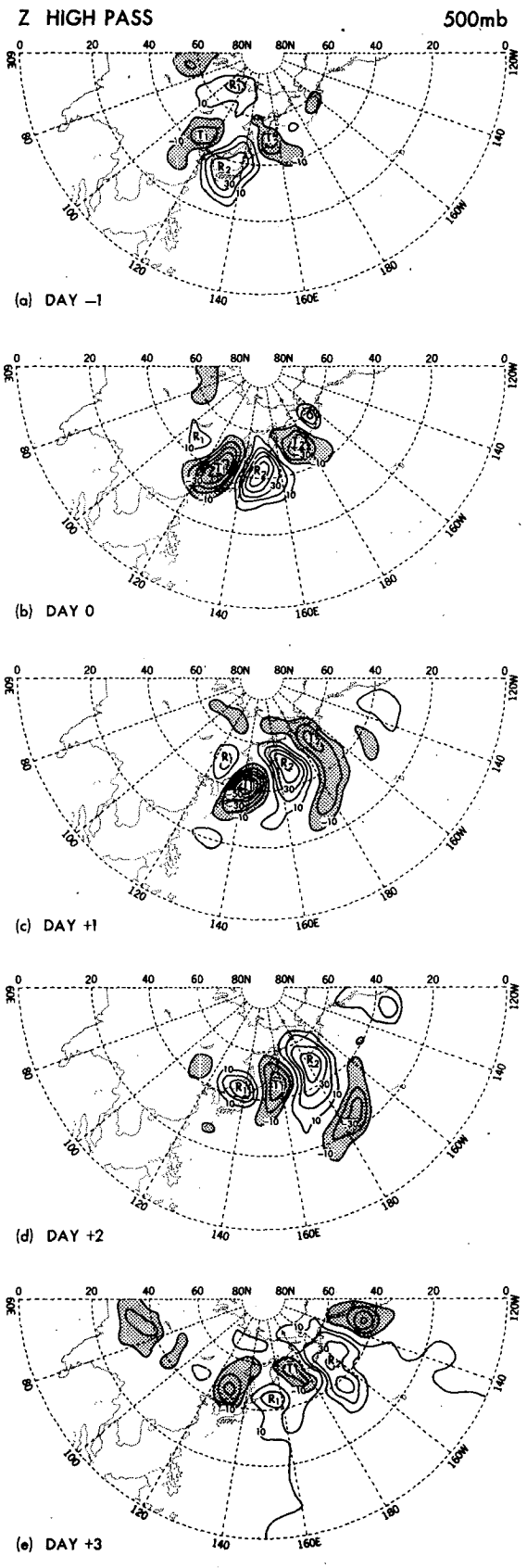

of the background flow illustrates vividly the steering effect of the latter on the path of the synoptic scale waves. Since patterns of both the seasonally averaged flow field and the cyclone tracks at 500 mb are qualitatively similar to the corresponding patterns at other pressure levels in the middle and upper troposphere, the steering effect noted here is probably discernible throughout the atmospheric column between 700 mb and the tropopause.

The temporal evolution of individual features along the storm track is further delineated by the Hovmöller diagram for high-pass filtered 500 mb height data shown in Fig. 7. Here the abscissa is the distance along the curved track drawn in Fig. 6, with the western and eastern ends of this track corresponding to the left and right edges of the plot, respectively. The prominent ridges and troughs are identified by the same labels as those used in Fig. 5. It is evident that R_2, T_1 and T_2 evolve through distinct stages of development during the 6-day period centered on the cold surge. These features develop rapidly between Day −2 and Day 0, with amplitudes peaking around Day +1, and begin to dissipate beyond Day +2. Hovmöller diagrams have been constructed for high-pass fluctuations of geopotential height and temperature at various levels between 1000 and 300 mb. These plots (not shown) are essentially similar to that presented in Fig. 7. As can be inferred from the slopes of the minimum and maximum axes in Fig. 7, the individual troughs and ridges progress along the curved track shown in Fig. 6 with an almost uniform phase speed of about 15 m s^{-1}. The appropriate steering level for the high frequency disturbances is hence located near 700 mb, where the prevalent wind speeds are closest to the phase velocity given here. Blackmon *et al.* (1984b) arrived at a similar conclusion after examining the spatial patterns of cross-correlation statistics for various lags.

The vertical structure of the high-pass fluctuations on Days −1 and +1 is depicted by the cross sections shown in Fig. 8, for geopotential height (a and b), temperature (c and d) and horizontal divergence (e and f). The midtropospheric troughs and ridges in Figs. 8a and b are labeled using the same nomenclature as the preceding diagrams. The sense of the vertical velocity may be inferred from Figs. 8e-f by noting that upward motion in the middle troposphere is associated with convergence near the surface and divergence at the tropopause level, and vice versa. On Day −1, the upper-level trough T_1 is situated over Korea and northeastern China, with a high pressure system di-

FIG. 5. Composite charts of the high-pass filtered 500 mb height fluctuations on (a) Day −1, (b) Day 0, (c) Day +1, (d) Day +2 and (e) Day +3. Contour interval is 10 m. The data have been weighted by the reciprocal of the sine of latitude (see text). Labels T_1, T_2, R_1 and R_2 indicate the positions of principal troughs and ridges at different times. The zero contour is omitted for clarity. Shading indicates negative values.

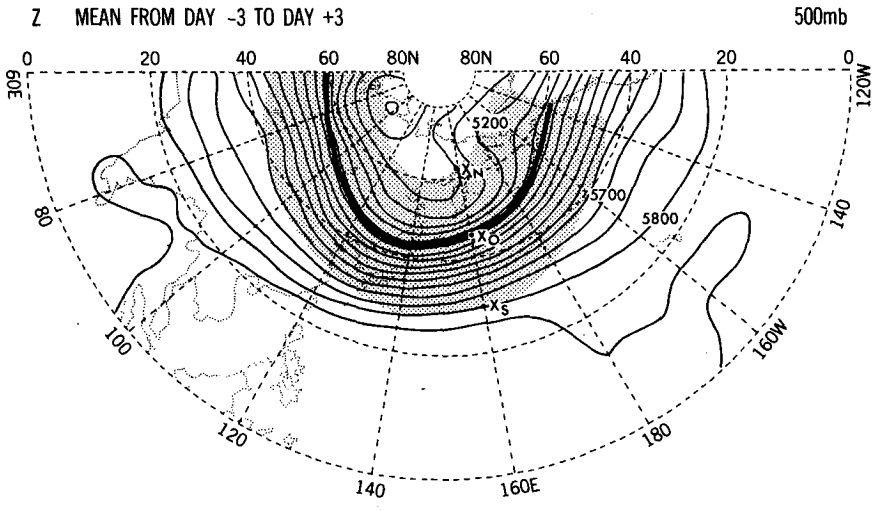

FIG. 6. Distribution of 500 mb height as obtained by averaging the composite charts for the period between Day −3 and Day +3. Contour interval is 50 m. The bold line in the shaded region represents the track of the principal high and low centers shown in Fig. 5. The shaded region and the labels X_S and X_N indicate the meridional extent used in computing volume integrals in the energy cycle (see Section 4b).

rectly underneath (Fig. 8a). This configuration is associated with a cold-air dome extending through the entire tropospheric column (Fig. 8c), and local subsidence prevails (Fig. 8e). On Day +1, the intensifying trough T_1 is located over Japan (see Fig. 5c), and the associated surface cyclone has advanced to the tip of the Kamchatka Peninsula. Both T_1 and the downstream ridge R_2 have acquired a pronounced westward

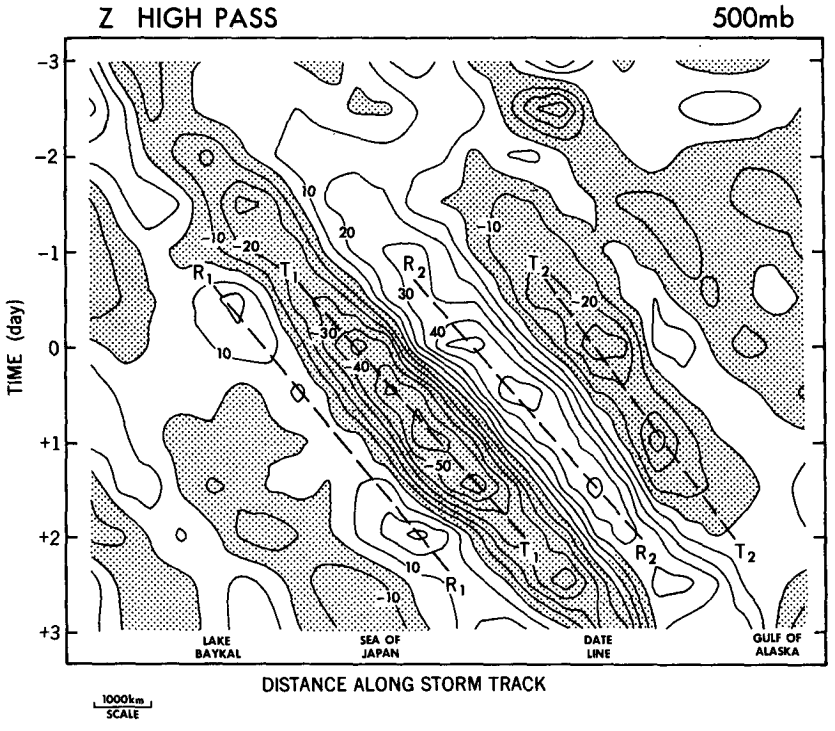

FIG. 7. Hovmöller diagram for high-pass filtered 500 mb height, weighted by the reciprocal of the sine of latitude. Contour interval is 10 m. Shading indicates negative values. The abscissa is the distance along the curved track shown in Fig. 6. The labels identifying principal troughs and ridges (T_1, T_2, R_1 and R_2) correspond to those in Fig. 5.

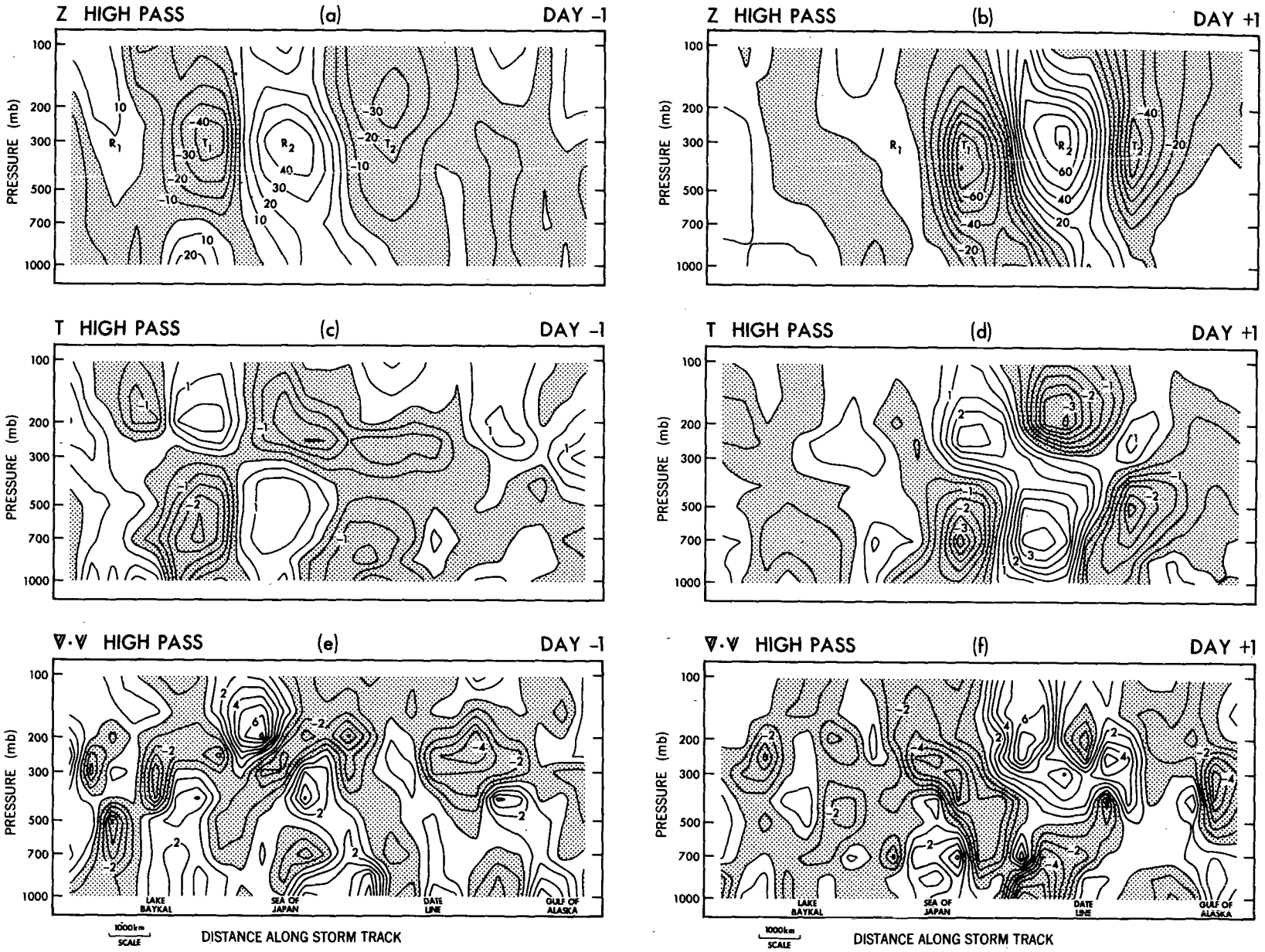
Z HIGH PASS (a) DAY -1
Z HIGH PASS (b) DAY +1
T HIGH PASS (c) DAY -1
T HIGH PASS (d) DAY +1
∇·V HIGH PASS (e) DAY -1
∇·V HIGH PASS (f) DAY +1
PRESSURE (mb)
100
200
300
500
700
1000
LAKE BAYKAL
SEA OF JAPAN
DATE LINE
GULF OF ALASKA
1000km SCALE
DISTANCE ALONG STORM TRACK

tilt with increasing height (Fig. 8b). At this time, a region of sharp temperature contrast near 700 mb is present over the western Pacific (Fig. 8d). Comparison between Figs. 8d and f reveals that a thermally direct tropospheric circulation has developed in the vicinity of this baroclinic zone, with ascent of warm air and descent of cold air. As T_1 and R_2 cross the Date Line during the following days (not shown), they gradually become more barotropic with a vertical structure similar to that of T_2 in Fig. 8b. Throughout the 6-day composite period considered here, the temperature fluctuations in the troposphere exhibit a strong negative correlation with those in the overlying stratosphere (Figs. 8c and d). Hence, in accordance with the hydrostatic relationship, the geopotential height perturbations attain maximum amplitudes in the upper troposphere. The evidence presented in this composite study is consistent with previous findings using cross-spectral techniques on the structural changes of high frequency eddies as they travel across the midlatitude oceans (Lau, 1979).

b. *Energetics*

The structural changes of the high-pass fluctuations in the course of a typical cold surge episode evidently have strong implications for their energetics. While a full treatment of the energy balance is not attempted here, we shall focus our attention on the temporal evolution of the vertically integrated quantities

$$A_E = \int \frac{T_h^2}{2\sigma}\, dp,$$

$$K_E = \frac{1}{g}\int \frac{u_h^2 + v_h^2}{2}\, dp,$$

$$C_A = -\int \frac{1}{\sigma}\left(u_h T_h \frac{\partial T_l}{\partial x} + v_h T_h \frac{\partial T_l}{\partial y}\right) dp,$$

$$C_K = -\frac{1}{g}\int \left(u_h u_h \frac{\partial u_l}{\partial x} + v_h u_h \frac{\partial u_l}{\partial y} + v_h u_h \frac{\partial v_l}{\partial x} + v_h v_h \frac{\partial v_l}{\partial y}\right) dp.$$

Here, A_E and K_E denote the available potential energy and kinetic energy of the high-pass eddies, respectively; C_A and C_K are measures of the conversion of available potential energy and kinetic energy, respectively, from the quasi-stationary flow (as represented by the low-pass filtered data) to the high-pass eddies; subscripts h and l denote high-pass and low-pass filtered data, respectively; σ is the areal average of the static stability parameter for the quasi-stationary flow, taken to be dependent on time and pressure only; and g is the gravitational acceleration. All other symbols are used in their conventional meteorological context, and the vertical integration is taken from 100 to 1000 mb.

The formulation used here needs to be distinguished from that of the conventional energy cycle (Lorenz, 1955). In the latter framework, atmospheric variables are partitioned into a zonally averaged component and an eddy component encompassing all deviations from the zonal mean. On the other hand, our study emphasizes local interactions between a quasi-stationary component (variables with subscript l), and a rapidly varying transient component (variables with subscript h). The present formulation is evidently more suited to investigations on circulation systems which are confined to certain geographical regions, and which exhibit several characteristic time scales. Simmons *et al.* (1983, Section 11b and Fig. 27) have advocated a similar breakdown of various quantities into a time-averaged component and a transient component for elucidating conversion processes associated with the barotropic instability of a zonally varying time-mean basic state.

A vigorous diagnosis of the energy conversion processes within a limited domain entails the computation of spatial averages of C_A and C_K, as well as certain terms involving boundary fluxes. As will be demonstrated later in this subsection (see Fig. 10), the geographical locations of the limited domains are chosen such that the most active disturbances reside in the interior of these domains, and the eddy processes at the boundaries of such domains are comparatively much weaker. We shall henceforth neglect the contributions of the boundary terms and focus our attention on C_A and C_K.

Prior to presenting the areal averages of C_A and C_K, it is nevertheless of some interest to examine how the synoptic features associated with the cold surges contribute locally to these conversions. Figure 9 shows the distributions of C_A (a and b) and C_K (c and d) on Days 0 and +1.5. The pattern for C_A on Day 0 (Fig. 9a) is characterized by a principal maximum sandwiched between a pair of secondary maxima. A principal maximum (centered at 45°N, 167.5°E) and a secondary maximum (centered at 40°N, 140°E) are also evident in the corresponding pattern on Day +1.5 (Fig. 9b). Comparison between Figs. 9a and 5b indicates that the principal maximum in C_A is situated between the trough T_1 and the ridge R_2, and that the secondary maxima are located just upstream of the troughs T_1 and T_2. The poleward transport of warm air ($v_h > 0$,

FIG. 8. The vertical structure of high-pass filtered fluctuations on Day −1 and Day +1 of (a) and (b) geopotential height, weighted by the reciprocal of the sine of latitude (contour interval 10 m); (c) and (d) temperature (contour interval 0.5°C); and (e) and (f) horizontal divergence (contour interval 1×10^{-6} s^{-1}). The ordinate in these plots is pressure and the abscissa is the distance along the curved track shown in Fig. 6. Shading indicates negative values. The labels identifying principal troughs and ridges (T_1, T_2, R_1 and R_2) correspond to those in Fig. 5.

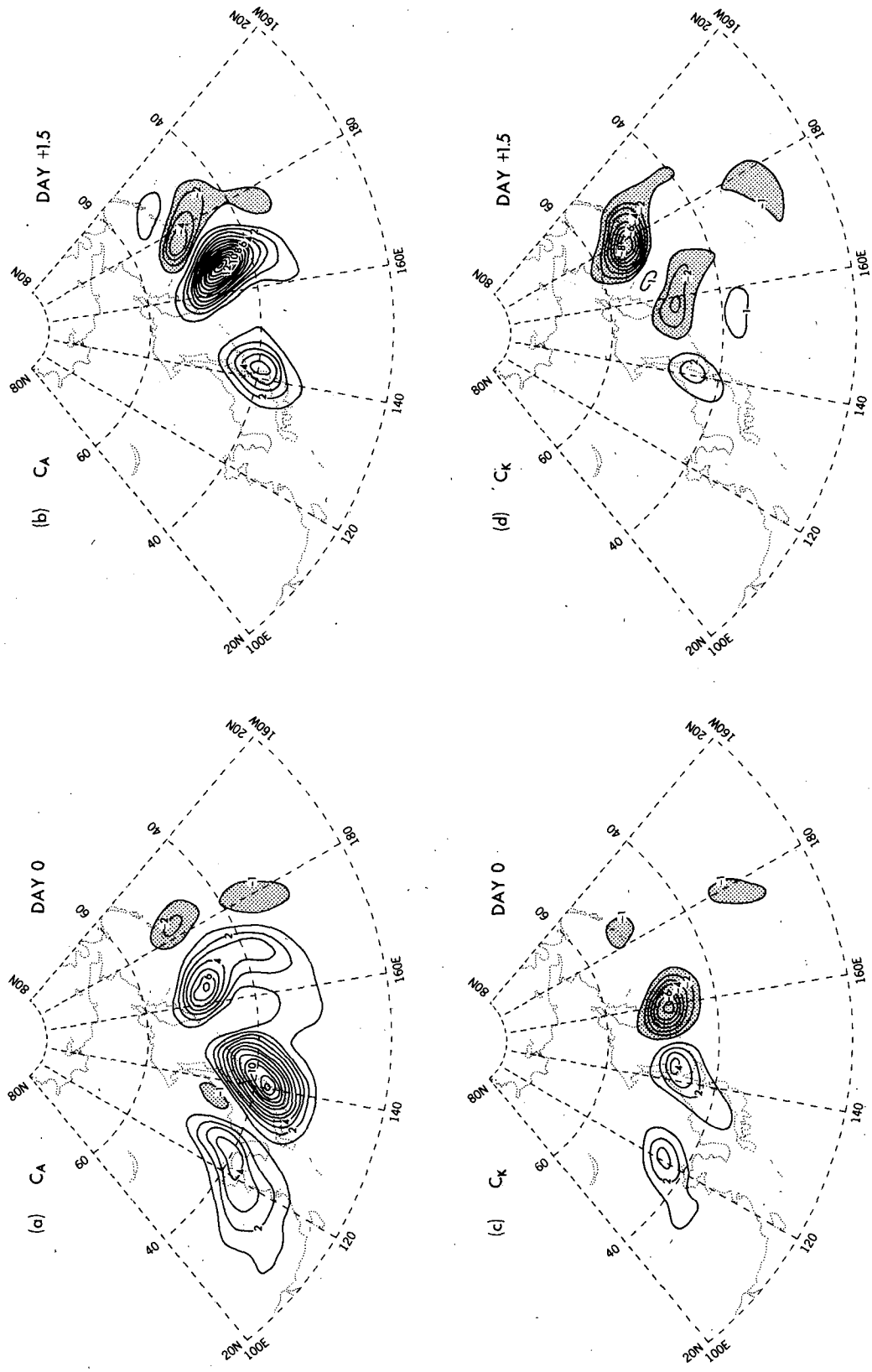

FIG. 9. Distributions on Day 0 and Day +1.5 of the vertically integrated conversion terms (a) and (b) C_A, and (c) and (d) C_K (see definitions in text). Contour interval is 1 W m^{-2}. Shading indicates negative values. Zero contour is omitted for clarity.

$T_h > 0$) is seen to be mainly responsible for the conversion of available potential energy, whereas the contribution of the equatorward transport of cold air ($v_h < 0$, $T_h < 0$) to C_A is relatively less significant.

Our computations indicate that $-v_h u_h \partial u_l / \partial y$ is by far the dominant term in the expression for C_K. The conversion of kinetic energy is hence essentially determined by the nature of the horizontal tilts of the high frequency disturbances in the vicinity of the Asian jet stream. Through much of the composite period, the jet axis over the domain of interest is located along the zonal belt between 30 and 35°N. In the region west of about 150°E, the prevalent southwest to northeast tilt of the eddies north of the jet (Fig. 5) is associated with positive C_K and hence barotropic growth (Figs. 9c and d). The eddies develop a southeast–northwest tilt farther downstream on the cyclonic side of the jet, and decay barotropically by feeding momentum back to the quasi-stationary flow ($C_K < 0$).

Most of the centers of extremum appearing in Fig. 9 are also recognizable in other such patterns throughout the entire period from Day −1 through Day +3. The tracks of these individual centers tend to be parallel to the storm track depicted in Fig. 6. The movement and temporal continuity of the principal features in Fig. 9 are illustrated in the Hovmöller diagrams in Fig. 10 for (a) C_A and (b) C_K. The value presented in Fig. 10 for any given point X_0 along the storm track represents the average of data at all grid points lying along the segment between X_S and X_N (see Fig. 6). The segment used here is the meridian intersecting X_0 and includes those points located within 15° latitude (north or south) from X_0. The area swept by the segments for different points along the storm track is depicted in Fig. 6 by shading. In computing the averages along individual segments, the data are weighted by the cosine of latitude. Also plotted in Fig. 10 are the positions of the major troughs and ridges, as inferred from the maximum and minimum axes in Fig. 7.

It is seen in Fig. 10a that the movement of the primary maximum in C_A follows closely the progression of T_1 and R_2 along the storm track. The high-pass fluctuations begin actively gaining available potential energy from the quasi-stationary flow on Day 0 when T_1 crosses the East Asian coast. Peak values of C_A are observed over the western Pacific on Days +0.5 to 1.5. Also distinguishable in Fig. 10a are the pair of secondary maxima in C_A located upstream and downstream of the principal maximum. The movement of these relatively weaker features is seemingly also associated with the migratory ridges and troughs.

The overall patterns in Figs. 9a, b and 10a indicate that efficient conversion of available potential energy from the time-mean flow to the transient eddies is realized only during certain time periods and over certain geographical regions. In particular, it is seen that much of the conversion occurs downstream of T_1 shortly after the polar outbreaks, whereas the values of C_A are negligibly small elsewhere in the space–time domain. We note further that the local maxima of C_A in Figs. 9a, b and 10a have typical magnitudes of 5–15 W m^{-2}, which are much larger than those of the corresponding quantity in the hemispherically averaged energy cycle (~1–2 W m^{-2}; see, e.g., Lau and Oort, 1982, Fig. 13). Hence it is likely that, although the midlatitude baroclinic disturbances accompanying the cold surges tend to be localized in both space and time, they still play a significant role in the global atmospheric energetics.

The pattern in Fig. 10b is characterized by positive C_K upstream of R_2 during Day −1.5 to Day +1, as well as negative C_K downstream of R_2 during Day −0.5 to Day +2.5. For the region located downstream of T_1 and upstream of R_2, the sign reversal of C_K (from positive to negative) on about Day +1.5 is probably associated with the change in horizontal tilt of T_1 as it approaches the Kamchatka Peninsula (compare Fig. 5c with Fig. 5d).

Plots analogous to those in Fig. 10 have been constructed for A_E and K_E (not shown). The temporal variation of the eddy energies is also primarily determined by the movement of the ridges and troughs, especially T_1 and R_2.

We shall conclude this section by describing the variation of certain areal averages of $A_E + K_E$, C_A and C_K during the 6-day composite period. Recalling that the averaging process has already been performed in the meridional direction while constructing Fig. 10, the desired measure for the present purpose may simply be obtained by averaging the data values along the abscissa in Fig. 10 for any given day. Instead of using data for the entire length of the storm track, the averages for a given time category are to be taken along that section of the track where the strongest eddy processes are taking place in the particular time category of interest. The position of such continuous sections is chosen to shift progressively eastward along the storm track from Day −3 to Day +3, thereby trailing in a Lagrangian fashion the eastward migration of the most active disturbances. However, we require that the width of these sections be the same for all time categories considered here. For $A_E + K_E$ and C_A, the two ends of the section chosen for any given day are indicated by the intersections of the pair of bold lines with the abscissa in Fig. 10a on that day. For instance, the section chosen for Day −1 extends from Lake Baykal to the International Date Line (refer to labels along the abscissa in Fig. 10b). In view of the different behavior of C_K upstream and downstream of the ridge R_2, two subdivisions are defined for this particular parameter. The extents of these subdivisions are similarly depicted by the bold lines in Fig. 10b. We shall refer to the areal averages of C_K for the eastern and western subdivisions as C_K^E and C_K^W, respectively. By limiting our attention to the domain where the most enhanced perturbations reside, we wish to extract the

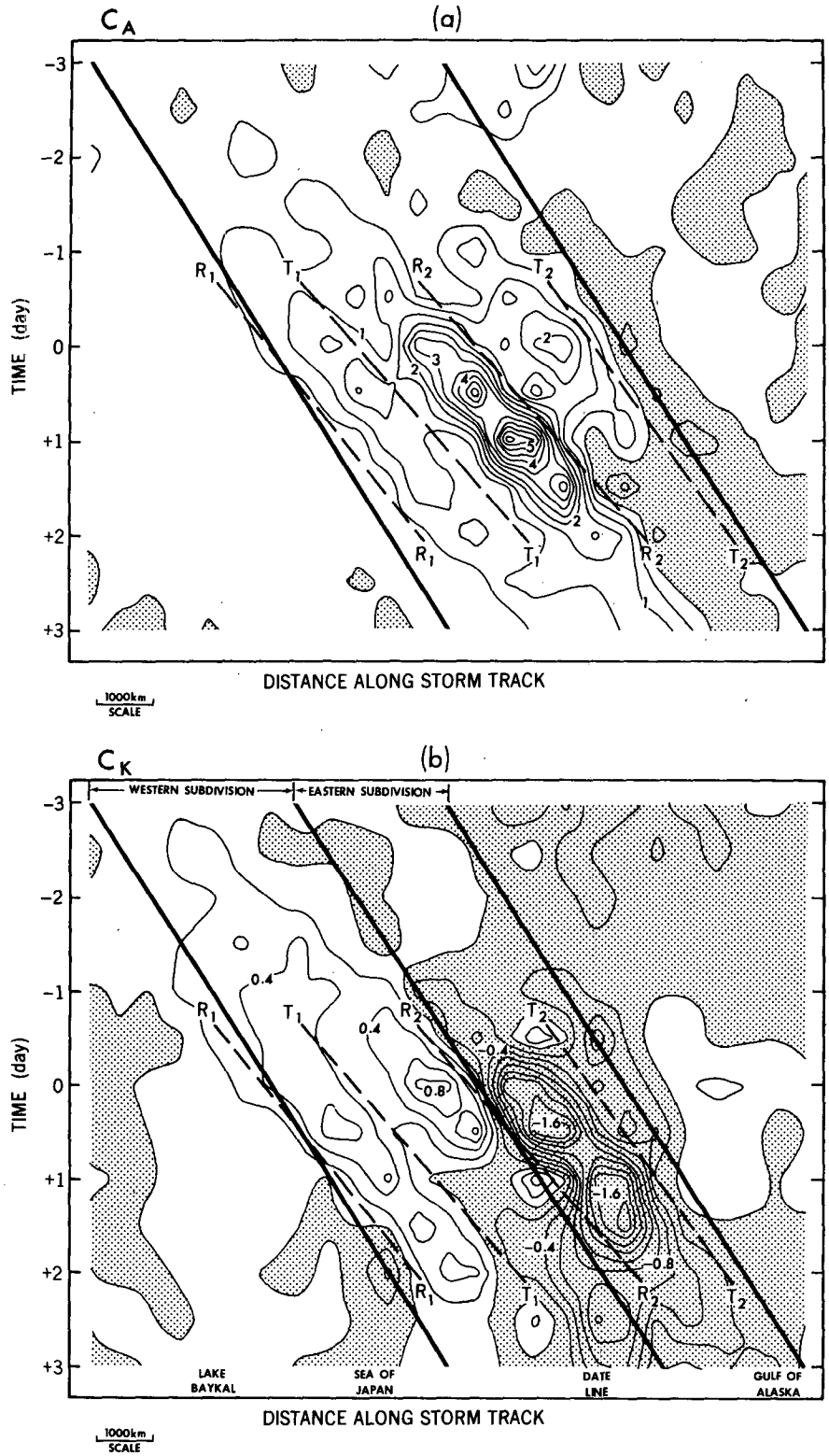

FIG. 10. Hovmöller diagram for (a) C_A (contour interval 0.5 W m^{-2}), and (b) C_K (contour interval 0.2 W m^{-2}). The abscissa is the distance along the curved track shown in Fig. 6. Shading indicates negative values. The values shown here are averages taken along finite sections of the meridians intersecting the grid points along the storm track (see text and Fig. 6). The propagation of the principal troughs and ridges, as inferred from the pattern in Fig. 7, is depicted by the dashed sloping lines. The bold lines define the boundaries of the segment along the storm track used for computing various terms in the energy cycle for a given time (see text and Fig. 11).

strongest possible signal on the temporal changes of various parameters of interest. Computations based on other configurations of these sections and subdivisions indicate that the qualitative results presented below are not particularly sensitive to the choices made.

The time series of areal averages of $A_E + K_E$, C_A, C_K^E and C_K^W, as computed using the procedure outlined above, are presented in Fig. 11. The temporal evolution of the individual quantities A_E and K_E (not shown) is similar to that of their sum $A_E + K_E$. There is a weak indication that the occurrence of the maximum in A_E leads that of the maximum in K_E by 0.5 day. The total eddy energy peaks on Day +1. The development phase of the disturbances prior to that time is accompanied by active baroclinic processes (C_A) and, to a much lesser extent, by barotropic processes in the western portion of the storm track (C_K^W). The magnitudes of $A_E + K_E$, C_A and C_K^W drop noticeably after Day +1, whereas the dissipative barotropic processes in the eastern part of the storm track (C_K^E) remain active through Day +2. The baroclinic growth and barotropic decay of synoptic scale waves described here lend some empirical support to the findings on the life cycles of nonlinear baroclinic waves reported in the modeling studies of Simons (1972), Gall (1976) and Simmons and Hoskins (1978).

5. Evolution of fluctuations with long time scales

The temporal development of circulation anomalies with time scales much longer than ~5 days is illustrated by the composite charts in Fig. 12, which show the patterns of low-pass filtered (see Section 2b) 500

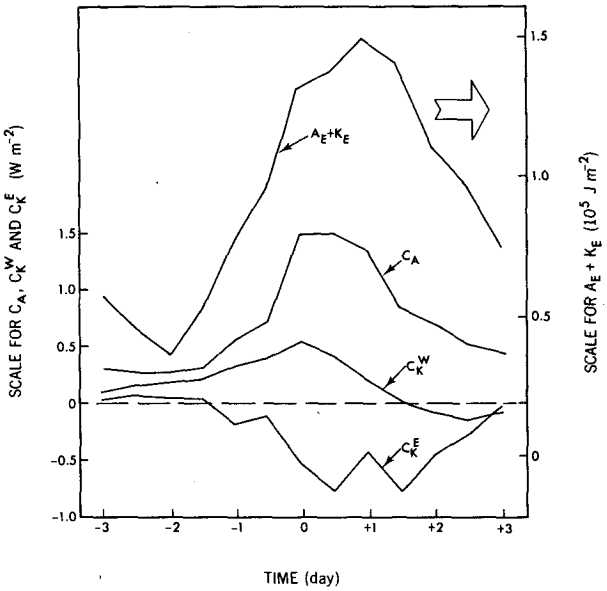

FIG. 11. Variation of areal averages of $A_E + K_E$, C_A, C_K^E and C_K^W during the 6-day composite period. See text for details of computation of these limited-area averages.

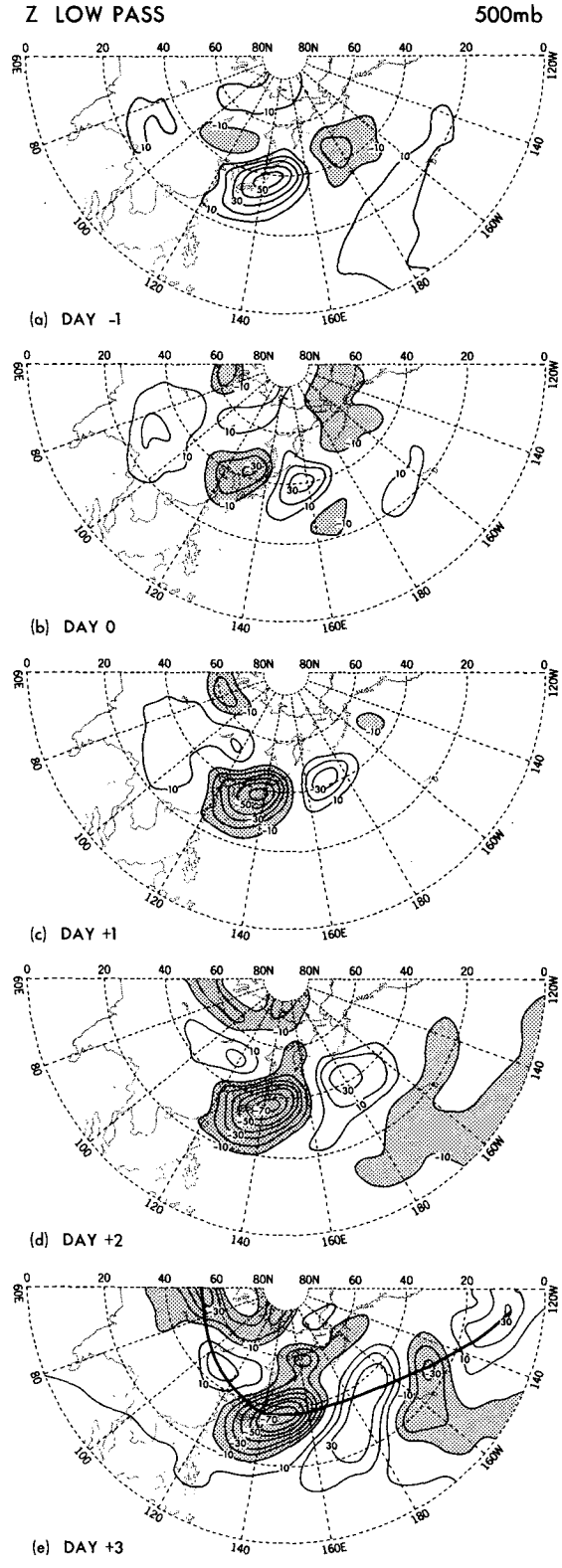

FIG. 12. As in Fig. 5, but for low-pass filtered 500 mb height fluctuations. The mean values for the period from Day −3 to Day +3 have been subtracted from the filtered data to obtain deviations. The bold line connecting the centers of extremum on Day +3 (e) is used for constructing the vertical sections in Fig. 13.

mb height data at 1-day intervals. In constructing these charts, the mean values for the 6-day composite periods centered on the cold surges (i.e., the values shown in Fig. 6) have been subtracted from the low-pass filtered data for individual days to obtain deviations. As for the high-pass filtered data shown in Fig. 5, the values presented here have been weighted by the latitude-dependent factor $\sin 45°/\sin\phi$. Comparison between the patterns in Figs. 5 and 12 on the respective days indicates that, on about Day 0, the geographical locations of individual high-pass features tend to coincide with the sites of the corresponding low-pass anomalies. The high-pass and low-pass fluctuations are also of comparable amplitudes at this time. Beyond Day 0, the slowly varying disturbances evolve in a manner quite different from that of the high frequency eddies. It is seen from Figs. 12c, d and e that amplification of the low-pass fluctuations continues through the second half of the 6-day composite period. As these disturbances advance toward the Pacific, they gradually become elongated in the zonal direction, and their overall horizontal extent increases. There is also evidence of a systematic movement toward the subtropical eastern Pacific. By Day +3, the features in the low-pass pattern (Fig. 12e) are distinctly stronger than those in the corresponding high-pass pattern (Fig. 5e), and two new features have developed at the eastern end of the wave train: a cyclonic center in the vicinity of Hawaii and an anticyclonic center at 10°N, 125°W. Also discernible in Fig. 12e is the preferential southwest–northeast tilt of the major features.

The tendency for the low-pass fluctuations to be elongated along the east–west direction has also been reported by Hoskins *et al.* (1983), based on anisotropy measures, and by Blackmon *et al.* (1984a), based on one-point teleconnection maps. The orientation of the train of low-pass fluctuations appearing in Fig. 12e bears some resemblance to that of the waveguide discussed by Blackmon *et al.* (1984a, Fig. 13b) for eddies with 10–30 day periods emanating from the entrance region of the Asian jet stream.

The vertical structure of the low-pass fluctuations on Day +3, when these disturbances attain maximum amplitudes and have spread from the interior of Asia to the subtropical Pacific, is depicted in Fig. 13 for (a) geopotential height and (b) temperature. It is seen from Fig. 13a that the low-pass filtered geopotential height fluctuations develop noticeable vertical tilts over eastern Asia and the western Pacific, whereas the disturbances over the central Pacific have a relatively more barotropic structure. The amplitudes of midtropospheric geopotential height fluctuations over the East Asian seaboard are much higher than those of the corresponding fluctuations at the surface, whereas the amplitudes of disturbances farther upstream and downstream exhibit less vertical variations. The strongest low frequency temperature fluctuations are located over the Eurasian land mass and the western Pacific (Fig. 13b). As for the high-pass data (Figs. 8c and d), an out-of-phase relationship exists between the temperature fluctuations in the troposphere and those in the lower stratosphere. There is a weak indication of a cold-core low structure in the vicinity of 25°N, 150°W.

Blackmon *et al.* (1979, Figs. 3 and 5) have examined the geographical variations in the vertical structure of slowly varying disturbances by mapping the temporal correlations and amplitude ratios between geopotential height fluctuations at different pressure levels. The findings reported therein are generally in agreement with the discussion of Fig. 13.

6. Discussion

In this study, the sequence of midlatitude events occurring prior to and following the onset of cold-air outbreaks over the East Asian seaboard are studied using composite techniques. The evidence presented here suggests that two distinct types of disturbances are particularly active during the cold surge periods. The first type, as revealed by the high-pass filtered data, has typical time scales shorter than $\sim$ 5 days. The meridional scale of these fluctuations is generally larger than the zonal scale. Their energetics are characterized by baroclinic growth and barotropic decay. The movement of these waves is characterized by continuous phase propagation along a well-defined midlatitude storm track extending from East Asia to the Aleutian Islands. The three-dimensional structure and energetics of the high-pass fluctuations described here reinforces the interpretation of such phenomena in terms of baroclinic instability, as given in previous observational studies on time-filtered circulation statistics (e.g., Blackmon *et al.*, 1977, 1984a; Lau, 1979). The temporal development of the energetics for high frequency waves (see Fig. 11) is also reminiscent of the life cycles of baroclinic waves in nonlinear numerical simulations (e.g., Simmons and Hoskins, 1978, Figs. 4 and 5), notwithstanding the considerable simplifications made in these modeling studies.

The second type of disturbance identified here has much longer time scales, and is discernible from the composite patterns for low-pass filtered data. Unlike the high-pass fluctuations, these low frequency perturbations are elongated in the zonal direction during the mature phase (see Fig. 12e), and tend to migrate toward the subtropical Pacific. Such equatorward penetration is mostly accomplished by successive development of new centers downstream of the primary disturbance located over the western Pacific. Analogous synoptic development associated with downstream amplification was noted much earlier by Namias and Clapp (1944), among others. The gross characteristics of the low-pass phenomena are basically similar to those of fluctuations with time scales between 10 and 30 days, as discussed by Blackmon *et al.* (1984a). The

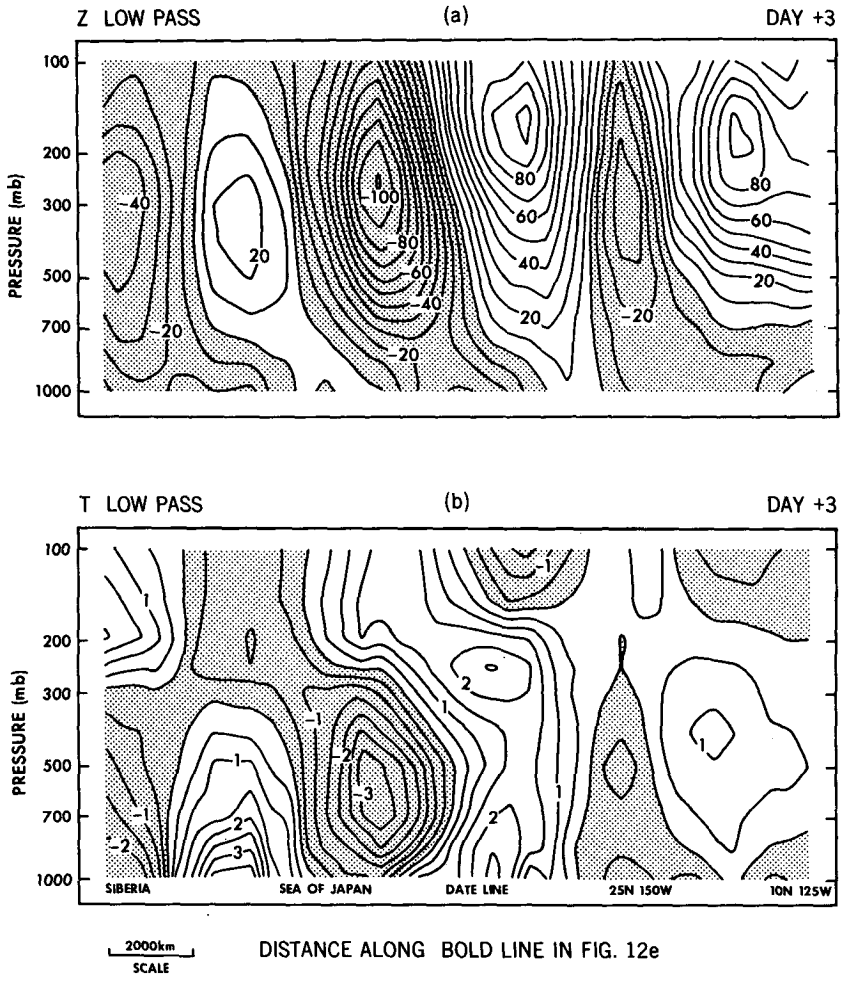

FIG. 13. Vertical structure on Day +3 of the low-pass filtered fluctuations of (a) geopotential height, weighted by the reciprocal of the sine of latitude (contour interval 10 m), and (b) temperature (contour interval 0.5°C). The ordinate is pressure and the abscissa is the distance along the bold line shown in Fig. 12e. Shading indicates negative values.

latter study interpreted such perturbations in terms of Rossby-wave dispersion along preferred ray paths. Theoretical treatment of energy dispersion phenomena in barotropic atmospheres has been given by Yeh (1949) and Hoskins *et al.* (1977).

The present composite study is primarily concerned with the structure and transport properties of disturbances related to cold-air outbreaks. It is worth noting, however, that the findings reported here are generally consistent with other diagnostic studies based on continuous climatological records (e.g., Blackmon *et al.*, 1977, 1984a,b). Since the latter investigations take into account disturbances which are associated with cold surges as well as those which are not, the overall agreement between their results and those described here suggests that the gross characteristics of disturbances accompanying cold-air outbreaks are probably rather representative of wintertime transient fluctuations in general.

The cold-core, almost equivalent barotropic feature in the vicinity of 25°N, 150°W (Fig. 13) seems to bear some resemblance to the synoptic pattern favorable for the genesis of subtropical cyclones ("kona" storms) near Hawaii. The tendency for the kona rainstorms to initiate as cold-core lows has been noted in the observational studies of Simpson (1952) and Ramage (1962). These authors emphasized local characteristics of the unstable environment in which these subtropical cyclones are embedded, and interpreted the evolution of such circulation features mostly in terms of *in situ* development. However, our results suggest that the origin of the large-scale circulation associated with kona storms might be traced upstream to cold-air outbreaks over East Asia several days earlier. The relative roles of the two mechanisms discussed here (local instability versus successive downstream amplification) in the formation and growth of kona storms require further study.

The short time intervals between cold surges as well as the weak intensity of several surges during the winter MONEX period preclude a meaningful investigation of the behavior of low-pass fluctuations much beyond 72 hours from the key dates. Further study of such interesting phenomena as the evolution of wave disturbances far upstream of the East Asian coast prior to the key dates,[1] and the formation of blocking ridges over the central and eastern Pacific after the outbreaks (as suggested by Joung and Hitchman, 1982 and Lau *et al.*, 1983), must await the analysis of weather records of longer duration and for periods with stronger outbreaks. The results presented here suggest that filtering in the temporal (and perhaps spatial) domains may aid in distinguishing various types of fluctuations.

Despite the notable differences in the behavior of the high-pass and low-pass fluctuations, it is clear that these two types of disturbances do not evolve independently of each other. The results in Fig. 6 demonstrate how the movement of the high-pass features is influenced by the curvature of the more slowly varying background flow. The active energy exchanges during the cold surges (Section 4b) are also indicative of the strong interactions between eddies of different time scales.

While this paper is mostly devoted to the description of dynamical processes involving various scales of atmospheric motions related to cold-air outbreaks, it should be emphasized that diabatic processes also play an important role in the course of these events. The notable influences of large scale sea–air interactions accompanying the intrusion of polar continental air masses over the relatively warm ocean surface in the western Pacific have been documented in many investigations, such as those associated with the Air Mass Transformation Experiment (e.g., Kung and Siegel, 1979).

The composite data displayed in this study are obtained by superposing 11 individual episodes with different intensities and synoptic situations. Hence the findings reported here necessarily pertain to a "typical" sequence of events in an arithmetically averaged sense. Whereas inspection of the synoptic charts for individual surges does indicate some degree of variability from case to case, most of the essential features in the composite results are also discernible in a majority of the episodes. Similarly, Joung and Hitchman (1982, Fig. 5) have demonstrated convincingly that the ridges and troughs associated with individual outbreaks are located at almost the same position and the same time relative to the key dates. The overall uniformity of the individual cases, together with the compatibility of our findings with those of other studies based on entirely different methods, further substantiates our earlier contention that the onset of a cold surge over East Asia is a useful index for observing the passage of various wave modes over that region.

Acknowledgments. We are particularly grateful to Academician T. C. Yeh for his continued interest in this work and for critically examining our results. We also wish to thank Drs. E. O. Holopainen, B. J. Hoskins, Y. Kurihara, J. D. Mahlman, A. H. Oort and the official reviewers for offering many constructive comments on the original manuscript. We are indebted to Messrs. R. Caverly and J. Sirutus for programming assistance, to Ms. J. Callan for typing, and to Messrs. J. Connor, W. Ellis and P. Tunison of the Geophysical Fluid Dynamics Laboratory for drafting the figures. NCL is supported at the Geophysical Fluid Dynamics Program by NOAA grant 04-7-022-44017.

[1] T. C. Yeh and collaborators (private communication, 1983) have noted that intense cold surges over China tend to be preceded by blocking phenomena in the vicinity of the Ural Mountains.

REFERENCES

Blackmon, M. L., J. M. Wallace, N.-C. Lau and S. L. Mullen, 1977: An observational study of the Northern Hemisphere wintertime circulation. *J. Atmos. Sci.*, **34**, 1040–1053.

——, R. A. Madden, J. M. Wallace and D. S. Gutzler, 1979: Geographical variations in the vertical structure of geopotential height fluctuations. *J. Atmos. Sci.*, **36**, 2450–2466.

——, Y.-H. Lee and J. M. Wallace, 1984a: Horizontal structure of 500 mb height fluctuations with long, intermediate and short time scales. *J. Atmos. Sci.*, **41**, 961–979.

——, ——, —— and H.-H. Hsu, 1984b: Time variation of 500 mb height fluctuations with long, intermediate and short time scales as deduced from lag-correlation statistics. *J. Atmos. Sci.*, **41**, 981–991.

Chang, C.-P., and K.-M. Lau, 1980: Northeasterly cold surges and near-equatorial disturbances over the winter MONEX area during December 1974. Part II: Planetary-scale aspects. *Mon. Wea. Rev.*, **108**, 298–312.

——, and ——, 1982: Short-term planetary-scale interactions over the tropics and midlatitudes during northern winter. Part I: Contrasts between active and inactive periods. *Mon. Wea. Rev.*, **110**, 933–946.

——, J. E. Erickson and K.-M. Lau, 1979: Northeasterly cold surges and near-equatorial disturbances over the winter MONEX area during December 1974. Part I: Synoptic aspects. *Mon. Wea. Rev.*, **107**, 812–829.

Frederiksen, J. S., 1983: Disturbances and eddy fluxes in Northern Hemisphere flows: Instability of three-dimensional January and July flows. *J. Atmos. Sci.*, **40**, 836–855.

Gall, R., 1976: Structural changes of growing baroclinic waves. *J. Atmos. Sci.*, **33**, 374–390.

GARP, 1980: Winter MONEX field phase report. FGGE operations report, Vol. 7, WMO, Section 1.

Holloway, J. L., 1958: Smoothing and filtering of time series and space fields. *Advances in Geophysics*, Vol. 4, Academic Press, 351–389.

Hoskins, B. J., A. J. Simmons and D. G. Andrews, 1977: Energy dispersion in a barotropic atmosphere. *Quart. J. Roy. Meteor. Soc.*, **103**, 553–567.

——, I. N. James and G. H. White, 1983: The shape, propagation and mean-flow interaction of large-scale weather systems. *J. Atmos. Sci.*, **40**, 1595–1612.

Joung, C. H., and M. H. Hitchman, 1982: On the role of successive downstream development in East Asian polar air outbreaks. *Mon. Wea. Rev.*, **110**, 1224–1237.

Kung, E. C., and A. J. Siegel, 1979: A study of heat and moisture

budgets in the intense winter monsoon over the warm ocean current. *J. Atmos. Sci.*, **36**, 1880–1884.

Lau, K.-M., and M. T. Li, 1984: The monsoon of East Asia and its global associations—A survey. *Bull. Amer. Meteor. Soc.*, **65**, 114–125.

——, C.-P. Chang and P. H. Chan, 1983: Short-term planetary-scale interactions over the tropics and midlatitudes during northern winter. Part II: Winter-MONEX periods. *Mon. Wea. Rev.*, **111**, 1372–1388.

Lau, N.-C., 1979: The structure and energetics of transient disturbances in the Northern Hemisphere wintertime circulation. *J. Atmos. Sci.*, **36**, 982–995.

——, and A. H. Oort, 1982: A comparative study of observed Northern Hemisphere circulation statistics based on GFDL and NMC analyses. Part II: Transient eddy statistics and the energy cycle. *Mon. Wea. Rev.*, **110**, 889–906.

Lorenz, E. N., 1955: Available potential energy and the general circulation. *Tellus*, **7**, 157–167.

Namias, J., and P. F. Clapp, 1944: Studies of the motion and development of long waves in the westerlies. *J. Meteor.*, **1**, 57–77.

Ramage, C. S., 1962: The subtropical cyclone. *J. Geophys. Res.*, **67**, 1401–1411.

Simmons, A. J., and B. J. Hoskins, 1978: The life cycles of some nonlinear baroclinic waves. *J. Atmos. Sci.*, **35**, 414–432.

——, J. M. Wallace and G. W. Branstator, 1983: Barotropic wave propagation and instability, and atmospheric teleconnection patterns. *J. Atmos. Sci.*, **40**, 1363–1392.

Simons, T. J., 1972: The nonlinear dynamics of cyclonic waves. *J. Atmos. Sci.*, **29**, 38–52.

Simpson, R. H., 1952: Evolution of the kona storm, a subtropical cyclone. *J. Meteor.*, **9**, 24–35.

Yeh, T.-C., 1949: On energy dispersion in the atmosphere. *J. Meteor.*, **6**, 1–16.